Reprint Series
29 November 1996, Volume 274, pp. 1495–1498

SCIENCE

The Clementine Bistatic Radar Experiment

S. Nozette,* C. L. Lichtenberg, P. Spudis, R. Bonner, W. Ort,
E. Malaret, M. Robinson, and E. M. Shoemaker

The Clementine Bistatic Radar Experiment

S. Nozette,* C. L. Lichtenberg, P. Spudis, R. Bonner, W. Ort, E. Malaret, M. Robinson, E. M. Shoemaker

During the Clementine 1 mission, a bistatic radar experiment measured the magnitude and polarization of the radar echo versus bistatic angle, β, for selected lunar areas. Observations of the lunar south pole yield a same-sense polarization enhancement around β = 0. Analysis shows that the observed enhancement is localized to the permanently shadowed regions of the lunar south pole. Radar observations of periodically solar-illuminated lunar surfaces, including the north pole, yielded no such enhancement. A probable explanation for these differences is the presence of low-loss volume scatterers, such as water ice, in the permanently shadowed region at the south pole.

The possibility of ice on the moon was suggested in 1961 (*1*). Volatiles degassed from the primitive moon or deposited on the lunar surface by cometary and asteroidal impacts might migrate to and collect in permanently shadowed cold traps near the lunar poles, where they could be stable over geologic time (*1–5*). Because these cold traps receive no direct solar illumination, and emit little radiation, they are difficult to observe from the Earth. Radar can identify deposits of frozen volatiles because, under certain conditions, they produce a unique radar signature (*6*). However, such radar observations may not be conclusive depending on the quantity of volatiles present, the nature of the surface, and the sensitivity of the measurements. Frozen volatiles have much lower transmission loss than silicate rocks, producing a higher average radar reflectivity than silicate rocks. Total internal reflection also preserves the transmitted circular polarization sense in the scattered signal. An opposition surge or coherent backscatter opposition effect (CBOE) (*7–12*) may also be observed as the phase, or bistatic angle β (Fig. 1), approaches 0. The CBOE requires scattering centers (cracks or inhomogeneities) imbedded in a low loss matrix such as ice (*7–9*). The preservation of the sense of polarization for CBOE has been observed in the laboratory using laser illumination of a particle suspension (*13, 14*). A high ratio of same sense to opposite sense polarization and high reflectivity has been detected by radar observations of the Galilean satellites of Jupiter (*15, 16, 17*), the residual south polar ice cap of Mars (*18*), portions of the Greenland ice sheet (*19, 20*), and the permanently shadowed polar craters of Mercury (*21–23*). These results are generally attributed to total internal reflection and/or CBOE produced by low loss frozen volatiles (*6*), although other mechanisms have been proposed (*24*). High-resolution ground-based synthetic aperture (monostatic) radar observations, from Arecibo, of the lunar south pole revealed some small anomalous same-sense polarization bright patches that are permanently shadowed (*25*). Brightening and enhancement of same sense polarization can be caused by double bounce reflections from large blocks or surface roughness. The presence of CBOE could distinguish brightening and polarization reversal produced by a low loss target from other scattering mechanisms. Bistatic radar measurements, using a spacecraft in orbit acting as the transmitter, can be used as a test for CBOE (*13, 14, 20*) by measuring the echo magnitude and polarization sense as a function of β.

The Clementine 1 mission (*26*) provided data on the environment and geology of the polar regions of the moon (*27, 28*). In the northern hemisphere, no large basin overlaps the polar area. The south pole, however, is located within the South Pole–Aitken basin (SPA), an impact crater over 2500 km in diameter and averaging 12 km deep near the center of the basin (*29*). The pole is about 200 km inside the rim crest of

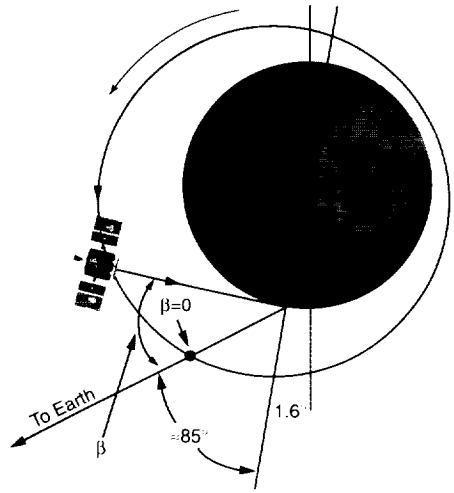

Fig. 1. Orbital geometry of the Clementine bistatic radar experiment. The lunar polar tilt relative to the ecliptic (1.6°), the lunar tilt toward Earth (−5°), and the bistatic angle β between spacecraft, lunar surface, and Earth receiver are shown.

S. Nozette, U.S. Air Force Phillips Laboratory, Space Experiments Directorate, 711 North Fayette Street, Alexandria, VA 22314, USA.
C. L. Lichtenberg, Naval Research Laboratory, Washington, DC 20375, USA.
P. D. Spudis, Lunar and Planetary Institute, Houston, TX 77058, USA.
R. Bonner and W. Ort, Protasis Incorporated, Alexandria, VA 22314, USA.
E. Malaret, Applied Coherent Technology, Herndon, VA 22070, USA.
M. Robinson and E. M. Shoemaker, U.S. Geological Survey, Flagstaff, AZ 86001, USA.
* To whom correspondence should be addressed.

the SPA. Because of its location inside this topographic low, the elevation of the south pole is likely to be several kilometers below the mean lunar radius, resulting in zones of permanent shadow (*27*, *28*). As the Clementine laser altimeter did not operate for lunar latitudes greater than 70°, there is no altimetry data for the polar regions. However, multiring basins tend to preserve concentric symmetry (*30*), thus the lunar south pole is estimated to lie about 5 to 8 km. below the highest point of the basin rim (*29*). If the elevation of the SPA rim crest on the near side is about 1 km, as suggested by the global map (*31*), then the pole would lie at an elevation of about −4 to −7 km. Study of the illumination conditions near the south pole of the moon during the mission reveal near constant illumination of several points within 30 km of the pole as well as darkness for other areas. Not all dark regions observed by Clementine are permanently dark, as the images were obtained during southern winter, near the time when the lunar spin axis obtained its maximum tilt away from the sun (1.6°). Initial analysis suggested that up to 30,000 km^2 near the south pole was dark during the mission (*27*). Further analysis of the Clementine images of the south pole taken over a two-month period showed that some of this region was illuminated for a small portion (<10%) of the lunar month. Images of the north pole taken on alternate orbits (10 hour intervals) during the first month and images of the south pole taken during the second month were registered and added together to make composite images showing the extent of illuminated and darkened areas (Fig. 2). These composite images show the extent of darkness near the south pole is much greater than that around the north pole. Mapping of the shadowed areas within a 2.5° latitude (75 km) radius circle of both poles reveals at least 6361 km^2 of darkness around the south pole while only 530 km^2 of darkness is measured around the north pole. A conservative analysis suggests an upper limit of 15,500 km^2 of south pole terrain is likely to be in permanent darkness. As the cold trap area at the south pole is more extensive than at the north pole, it would be expected (*2*) to retain more trapped volatiles.

In April 1994, during the times when the Earth passed through the Clementine orbital plane, the lunar axial tilt toward the Earth as viewed from the NASA Deep Space Network (DSN) was relatively large (4.5° to 5.5°). This favorable alignment occurred once for each pole during the month. At these times the spacecraft, lunar target, and Earth-based receiver were coplanar with the spacecraft orbital plane, and included the polar $\beta = 0$ condition (Fig. 1). Clementine transmitted an unmodulated S-band (2.273 GHz, 13.19 cm wavelength) right circular polarization (RCP) signal with a net power of about 6 W through its 1.1 m high gain antenna (HGA), toward a specific lunar target. One of the DSN 70-m antennas served as a receiver. On 9 and 10 April 1994, bistatic radar observations were made of the south pole region during orbits 234, 235, 236, and 237. On 23 and 24 April 1994, observations of the north pole were conducted on orbits 299, 301, and 302. Analytical results for orbits 234, 235, 301, and 302 are presented here. The other orbits had systematic errors originating in the spacecraft and the ground stations that made the data unusable. Interpretation of the surface physical properties involved comparison of the measured echo components with scattering models (*32*). In the initial analysis, the polarization ratio was compared to β and local surface angle of

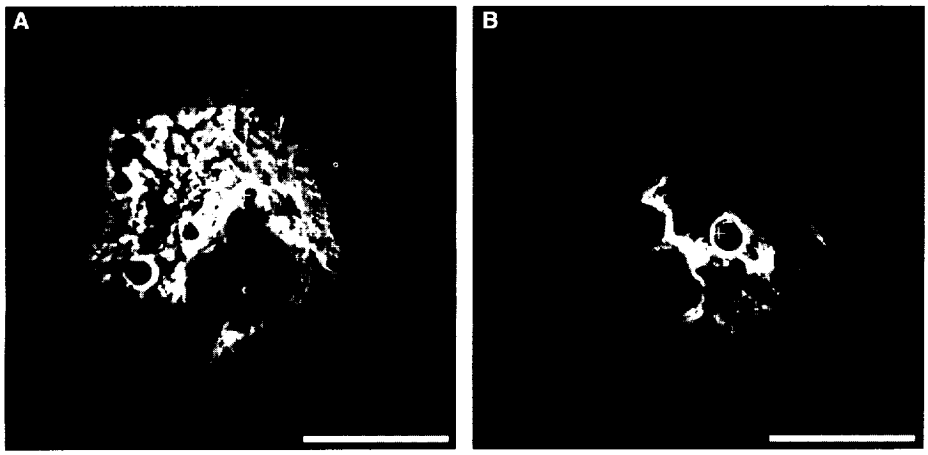

Fig. 2. Composite Clementine orbital images of the poles of the moon, where more than 50 separate images have been summed together over one lunar day. In these views, areas of near permanent illumination are white and areas of near permanent darkness are black. Within 100 km of each pole, the south pole (**B**) shows considerable darkness (= cold traps) whereas the immediate surroundings of the north pole (**A**) show at least an order of magnitude greater illumination, and are therefore warmer. The scale bar is 100 km.

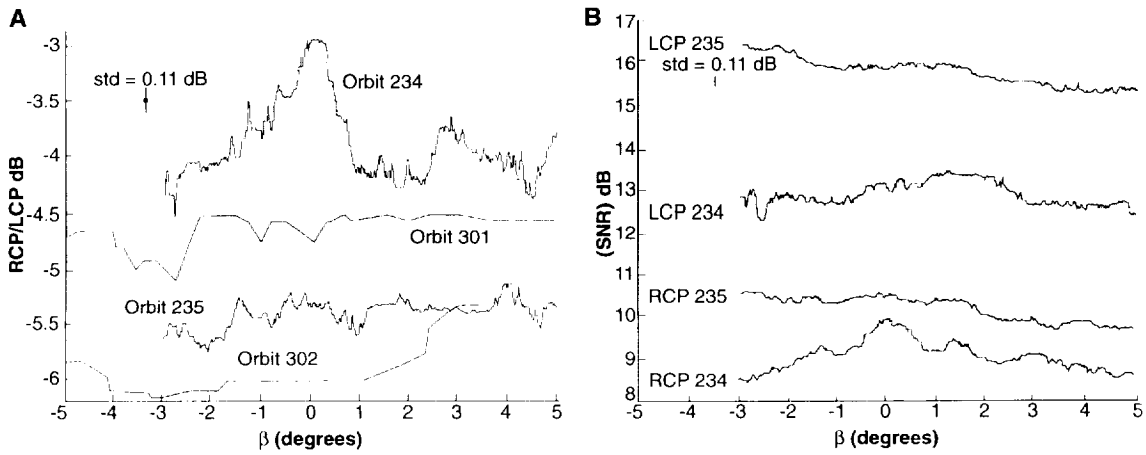

Fig. 3. (**A**) Circular polarization ratio (RCP/LCP) as a function of β for orbit 234 for a 2.5° radius latitude band centered on the lunar south pole and for orbit 235, for a 2.5° radius periodically illuminated band centered at 82.5°S, and for orbits 301 and 302, originating from a 2.5° radius band centered at the north pole. The area sampled is approximately 45,000 km^2 (orbits 234, 301, and 302) to 170,000 km^2 (orbit 235). (**B**) Individual polarization channel (RCP and LCP) echo power response used on a frequency bin-by-bin basis to compute the orbit 234 and 235 polarization ratios.

incidence (33). The scattering values presented represent regional averages. The normalized radar backscatter cross section (radar cross section per unit area) was estimated from the radar equation (34) and specific areas illuminated on the lunar surface. Typical values of normalized radar cross section derived from Clementine data for the near-polar regions, −80°(S) to −82.5° (S) (84° angle of incidence, $\beta = \pm 1°$), are −29 dB LCP (left circular polarization) and −33.5 dB RCP, consistent with previous work (25). During orbit 234 the $\beta = 0$ track (the locus of $\beta = 0$ points) and the center of the HGA beam were close (within 0.5° of each other and the south pole) which provided for good illumination of the entire permanently shadowed south pole region at the $\beta = 0$ condition. Orbit 235 has no $\beta = 0$ points near the south pole and is representative of periodically solar illuminated lunar surface. A noticeable peak in RCP/LCP occurs around $\beta = 0$ for the orbit 234 Doppler bins contained within a 2.5° radius band centered on the lunar south pole (Figs. 3 and 4). Orbit 235 yielded no discernible enhancement in latitude bands that exclude the south pole region (Fig. 3). The peak in the RCP/LCP ratio observed in orbit 234, at $\beta = 0$, is due to enhanced power received in the RCP channel (Fig. 3) as opposed to a reduction in LCP, as seen at $\beta \sim 2.5$ to 3.0°. No statistically significant enhancement was observed in orbit 234 LCP (35).

During orbits 301 and 302 the spacecraft was roughly four times closer to the lunar north pole surface at $\beta = 0$ than during the south pole observations. The corresponding antenna pattern had a proportionally smaller footprint, and the incident power density was roughly an order of magnitude greater than for the lunar south pole. More sensitivity is therefore expected in detecting scattering enhancement. The lunar north pole observations showed no statistically significant polarization enhancements at $\beta = 0$ (Fig. 3). These observations were averaged over a latitude band of 2.5° radius, centered on the north pole, containing an area comparable with the orbit 234 south pole observations. As the spacecraft velocity was greater near the north pole there are fewer $\beta = 0$ points in orbits 301 and 302. This produces flatter curves due to the filtering process (Fig 3).

Clementine polar observations were conducted at incidence angles of 82° to 90°. High incidence angle scattering is difficult to predict and can exhibit unusual behavior due to shadowing, diffraction, and multiple scattering effects (36). However no polarization ratio enhancement was observed on orbits 301 and 302, which had similar high incidence angle geometry and greater surface power illumination than orbits 234 and 235. Additionally, orbits 234, 235, 301, and 302 were re-analyzed, independently of β, to include only target areas at high local incidence angles (82° to 90°). Only orbit 234 showed an enhanced polarization ratio at high local incidence angles, which independently corresponds to south pole illumination at small β. All other orbits exhibited lower polarization ratio and no local angle of incidence dependent RCP/LCP enhancements. Statistical analysis (37) yields only a small probability (<5%) that the polarization ratio enhancement on orbit 234 is due to random variation in the data (Table 1), and is probably not attributable to angle of incidence.

It is not certain whether the enhancement seen in orbit 234 is due to CBOE or some other scattering effect. The CBOE peak usually predicted from lossless volume scattering should be much narrower (<0.1°), and also show a larger enhancement in RCP and LCP, than was observed (7–12, 23). There are several possible explanations for these observations, including the possibility that they are not due to CBOE from ice deposits. The orbit 234 data have been averaged over a large area of lunar surface (45,000 km^2) of which 14 to 33% is permanently shadowed (Fig. 4). If the putative ice deposits are small and patchy, the magnitude of the polarization reversal will be muted by reflections from the larger surrounding lunar surface area. Rocky lunar regolith may cover and be mixed with any ice deposits, further reducing the peak amplitude by increasing loss in the medium. Using the observed orbit 234 maximum, and median RCP/LCP ratios (Fig. 3 and Table 1), and methods used to estimate the extent of the Mercury polar deposits (23), we estimate the pure ice equivalent area of putative south pole ice deposits to be on the order of 0.2 to 0.3% of the observed region, or approximately 90 to 135 km^2. This area is consistent with small patches of high (≥1) RCP/LCP surface observed from Arecibo (25). The estimate may be a lower limit, as the viewing geometry does not allow observation of the deepest parts of the shadowed terrain. The broad orbit 234 RCP/LCP peak and the low value of RCP/LCP (<1) are consistent with rigorous theoretical calculations of CBOE for measurements made at grazing incidence angles, assuming wavelength scale scatterers imbedded in a lossy medium (7–12). The observed orbit 234 RCP peak width and magnitude is predicted by CBOE theory if the scattering centers are nonspherical (11) and cover only a fraction of the sampled area. In this case the predicted LCP peak amplitude would be significantly smaller and its width much larger than the observed orbit 234 RCP peak (12), and is not observable in the Clementine data owing to the inherent fluctuation of the much larger LCP background. This does not preclude the existence of a number of small scattering areas with RCP/LCP ≫ 1 and corresponding sharper LCP peaks that cannot be resolved in the data. These assumptions are geologically realistic for patchy, dirty ice. Other scattering mechanisms (roughness, double bounce) might explain the observed south pole RCP enhancement. However, the Clementine bistatic radar data only show this enhancement around $\beta = 0$ in an area at the lunar south pole containing at least 6361 km^2 of permanently shadowed

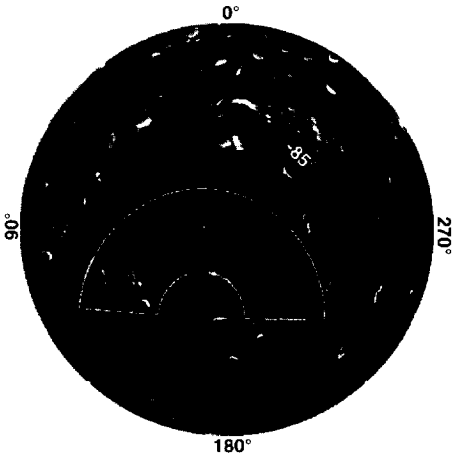

Fig. 4. Clementine mosaic of the south pole region of the moon showing area sampled on orbit 234.The white outline indicates the nominal area at the time of peak RCP response on orbit 234, as shown in Fig. 3. The limits of this area are defined by contours of constant Doppler shift of the received signal and the RF terminator on an idealized spherical moon. The spread of Doppler shift was chosen to maximize the fraction of permanently shadowed ground in the area sampled. On the actual moon, the true boundaries are irregular, owing to topography, and the fraction of the sampled area occupied by permanently shadowed ground probably is higher than in the idealized case.

Table 1. Circular polarization ratio (RCP/LCP) median value with 95% confidence interval for data sorted as a function of incidence angle, not as a function of β. All frequency bins representing 82° to 90° angle of incidence are included and presented as a median value. Because the orbit 234 RCP/LCP ratio is statistically greater than the other orbits, it is unlikely that this larger ratio would be found for other orbits when sorted on the basis of high angle of incidence.

Orbit	RCP/LCP median value (dB)
234	0.449 + 0.019 (3.476 ± 0.178)
235	0.325 + 0.011 (4.885 + 0.151)
301	0.354 ± 0.014 (4.512 ± 0.171)
302	0.318 · 0.012 (−4.978 ± 0.166)

terrain. Clementine bistatic radar data taken from other, intermittently sunlit areas with similar geometry, and subjected to the same data reduction process, show no evidence of such an enhancement. This leads to the conclusion that the scattering mechanism responsible for the orbit 234 enhancement is associated with the permanently shadowed terrain, which is suggestive of a muted CBOE originating from small patches of ice (and/or other frozen volatiles) covered and mixed with rocky material.

REFERENCES AND NOTES

1. K. Watson, B. C. Murray, H. Brown, *J. Geophys. Res.* **66**, 3033 (1961).
2. J. R. Arnold, *ibid.* **84**, 5659 (1979).
3. D. A. Paige, S. E. Wood, A. R. Vasavada, *Science* **258**, 643 (1992).
4. A. P. Ingersoll, T. Svitek, B. C. Murray, *Icarus* **100**, 40 (1992).
5. J. R. Salvail and F. Fanale, *ibid.* **111**, 441 (1994).
6. S. J. Ostro and E. M. Shoemaker, *ibid* **85**, 335 (1990).
7. K. J. Peters, *Phys. Rev.* **46**, 801 (1992).
8. S. Etemad *et al.*, *Phys. Rev. Lett.* **59**, 1420, (1987).
9. M. I. Mishchenko, *Astrophys. Space Sci.* **194**, 327 (1992).
10. F. F. Gorodnichev, S. L. Dudarev, D. B. Rogozkin, *Phys. Lett. A* **144**, 48 (1990).
11. M. I. Mishchenko, *J. Opt. Soc. Am.* **A 9**, 978 (1992).
12. ———, *Earth Moon Planets* **58**, 127 (1992).
13. B. Hapke, *Icarus* **88**, 407 (1990).
14. ——— and D. Blewitt, *Nature* **352**, 46 (1991).
15. D. B. Campbell *et al.*, *Icarus* **34**, 254 (1978).
16. R. M. Goldstein and R. R. Green, *Science* **207**, 179 (1980).
17. S. Ostro, in *Satellites of Jupiter*, D. Morrison, Ed. (Univ. of Arizona Press, Tucson, 1982).
18. D.O. Muhleman, B. J. Butler, A. W. Grossman, M. A. Slade, *Science* **253**, 1508 (1991).
19. E. J. Rignot, S. J. Ostro, J. J. van Zyl, K. C. Jezek, *ibid.* **261**, 1710 (1993).
20. E. J. Rignot, *J. Geophys. Res.* **100**, 9389 (1995).
21. J. K. Harmon *et al.*, *Nature* **369**, 213 (1994).
22. M. A. Slade, B. J. Butler, D. O. Muhleman, *Science* **258**, 635 (1992).
23. B. J. Butler, D. O. Muhleman, M. A. Slade, *J. Geophys. Res.* **98**, 15003 (1993).
24. V. Eschleman, *Science* **234**, 587 (1986).
25. N. J. S. Stacy, thesis, Cornell University (1993).
26. S. Nozette *et al.*, *Science* **266**, 1835 (1994).
27. E. M. Shoemaker, M. S. Robinson, E. M. Eliason, *ibid.*, p. 1851.
28. P. D. Spudis *et al.*, *Lunar Planet. Sci.* **XXVI**, 1339 (1995).
29. P. D. Spudis *et al.*, *Science* **266**, 1848 (1994)
30. P. D. Spudis, in *The Geology of Multi-ring Impact Basins* (Cambridge Univ. Press, Cambridge, 1993).
31. M. T. Zuber *et al.*, *Science* **266**, 1839 (1994).
32. R. A. Simpson, *IEEE Trans.* **GRS-31**, 465 (1993).
33. Analysis was conducted using fast Fourier transform (FFT) techniques. The target area is isolated by Doppler shift, which relates bands of constant frequency to a set of lunar ground locations (the $\beta = 0$ track). The ground points were close enough in distance to include all of the bands of constant frequency in the selected area. Repeat responses were filtered out. The analyses to extract radar scattering information from local regions on the surface were performed by sorting the Doppler data according to the parameter of interest. Typical frequency domain transform parameters used were 1 to 4 seconds of noncoherent averaging, 4096 to 16,384 points per FFT, a von Hann time data window without zero-padding, and magnitude-only (power) data stored in double precision output.
34. J. V. Evans and T. Hagfors, Eds., *Radar Astronomy* (McGraw-Hill, New York, 1968).
35. The effective system noise temperature baseline was estimated by comparing measured noise from the zenith (20 K), moon center (235 K), and lunar poles (90 K). Measurements of ambient temperature microwave resistors added further corroborating measurements to the set of calibration data. The noise baseline, when considered against the recorded attenuator values, was used to calibrate the amplitude of the data files into units of signal-to-noise ratio (SNR). Calibration to flatten the frequency response variation arising from receiver filters was performed using noise-only segments of data. The calibrations included: linear gain change, nonlinear gain change, recording channel frequency response, system noise temperature changes, erroneous data bridgeover, transmitter frequency variation, transmitter power variation, and antenna pointing. A small amount of corrupted data is inevitably recorded. The short periods of corrupted data were flagged and suppressed during subsequent analyses. Spacecraft attitude files were corrected for known timebase and pointing systematic errors. One-way light-time propagation delay effects were included. Systematic errors that simultaneously affect the absolute baseline or bias measurement of each polarization channel were estimated to be less than ± 2 dB. Systematic errors in the ratio measurements are estimated at ± 0.25 dB. The systematic errors common to both channels are suppressed when considering the ratio. Thermal noise variation is negligible because several hundred to several thousand frequency bins were averaged together, each having a thermal SNR greater than 10. Target speckle variation is believed to be the dominant stochastic error source. The mean value and error bars given in Fig. 3 are derived by reducing the data set standard deviation by the square root of the number of noncoherently averaged samples represented by each point on the plot. The use of noncoherently averaged FFTs and numerous frequency bins reduced this variation to about ± 0.1-0.2 dB standard deviation. Median filtering was used. Due to the time sampling, regional averaging, and spacecraft system characteristics the resolution in β is $\pm 0.2°$. Due to Doppler bin migration (± 1 bin), phase noise of the spacecraft oscillator (± 2 bins), and FFT windowing effects (± 2 bins), the Doppler band regions have an estimated rms resolution uncertainty of about ± 25 km at $-80°$ latitude, for the 16,384 point FFT data files.
36. L. Tsang, J. A. Kong, R. T. Shin, *Theory of Microwave Remote Sensing* (Wiley-Interscience, New York, 1985).
37. A standard analysis of variance (ANOVA) for unbalanced design was performed on the data from each orbit. ANOVA tests the null hypothesis that the means are the same and only appear different in measurement because of random fluctuations in the data. This analysis tests the statistical significance of the differences among the means. The data represented target return bins corresponding to angles of incidence greater than 82°.

38. The authors thank the NASA/JPL and Deep Space Network individuals who supported and helped carry out these observations, in particular S. Asmar; the Clementine lunar operations team led by T. Sorensen, assisted by R. Campion and T. Tran; P. Rustan of the U.S. Air Force, the Clementine 1 program manager, D. Duston of BMDO, and L. Wood of LLNL; and R. Simpson and G. Pettengill for review and insight. Funding for this work was provided by the Department of Defense, including the Ballistic Missile Defense Organization, the Naval Research Laboratory, the U.S. Air Force Phillips Laboratory Space Experiments Directorate, the Department of Energy, Lawrence Livermore National Laboratory, and NASA. This paper is Lunar and Planetary Institute contribution 899.

3 June 1996; accepted 22 October 1996